Earth and Planetary Science Letters 363 (2013) 231–241

Contents lists available at SciVerse ScienceDirect

Earth and Planetary Science Letters

journal homepage: www.elsevier.com/locate/epsl

Earthquake nucleation and triggering on an optimally oriented fault

Carl Tape [a,*], Michael West [a], Vipul Silwal [a,b], Natalia Ruppert [a]

[a] Geophysical Institute, University of Alaska, Fairbanks, Alaska, USA
[b] Indian Institute of Technology, Kharagpur, India

ARTICLE INFO

Article history:
Received 24 August 2012
Received in revised form
28 November 2012
Accepted 29 November 2012
Editor: P. Shearer
Available online 26 January 2013

Keywords:
earthquake triggering
earthquake nucleation
stress
strain

ABSTRACT

Seismic surface waves from large, distant earthquakes commonly trigger smaller earthquakes. However, delay times of hours to days between the surface waves and the triggered earthquakes weaken the causal connection. Furthermore, when there is no delay, the triggered earthquakes are typically too small or too obscured to obtain reliable source mechanisms. We present observations of instantaneous triggering of a strike-slip earthquake in central Alaska. Shear strain from the optimally aligned teleseismic Love wave induced a 24 s exponential foreshock signal leading to the triggered earthquake. This nucleation phase, and the alignment of the triggered earthquake source mechanism with the teleseismic stress field, reveal the behavior of an existing fault under well-calibrated strain conditions. The Alaska earthquake provides the first observation of combined nucleation and triggering, and it suggests that transient stresses during nucleation may influence the subsequent earthquake rupture. Laboratory and theoretical studies of nucleation and triggering may help discriminate between different interpretations for the Alaska earthquake.

1. Introduction

The process and timing of earthquake nucleation is unknown, in part due to lack of information describing the heterogeneity of structure and stress at seismogenic depths ($\sim 5-25$ km). Borehole measurements provide direct constraints on the state of stress at isolated locations and depths (Zoback et al., 1987; Lockner et al., 2011), while exhumed faults provide insight into the length scales of complexity that might be more relevant to nucleation processes (Scholz, 2002; Sagy and Brodsky, 2009). However, a complete characterization of subsurface faults is untenable; indeed, even in controlled laboratory experiments it is challenging to characterize frictional properties between two materials (Ben-David et al., 2010).

Observational evidence for nucleation and triggering provides insights into the physical conditions under which an earthquake occurs. There has been limited observational evidence for a nucleation phase, that is, for waveforms prior to the P arrival that hint at the earthquake to occur (Iio, 1995; Ellsworth and Beroza, 1995; Beroza and Ellsworth, 1996; Mori and Kanamori, 1996). Using a single station, Bouchon et al. (2011) reanalyzed the foreshocks from the 1999 M_w 7.6 Izmit earthquake reported by Özalaybey et al. (2002). They identified a 44-min foreshock sequence and attributed it to repeated rupturing of the same patch by fault creep. The final foreshock preceded the M_w 7.6 mainshock (P) by 0.07 s.

There has been ample evidence of smaller ($M < 3$), remotely triggered earthquakes following the passage of surface waves from larger events (Hill et al., 1993; Gomberg et al., 2004; West et al., 2005; Freed, 2005; Hill, 2008; Velasco et al., 2008; Parsons and Velasco, 2011; Wu et al., 2011). A global survey revealed that dynamic triggering of earthquakes from surface waves, notably Love waves, is common (Velasco et al., 2008). Seismologists have identified triggering of related sources such as creep and tremor from volcanic and non-volcanic regions (Rubinstein et al., 2007; Miyazawa and Brodsky, 2008; Shelly et al., 2011). Results from triggering studies indicate that dynamic stresses of a few kilopascals are sufficient to initiate earthquakes on critically loaded faults. The delay times between the stress perturbation and the triggered event have led to a variety of proposed mechanisms (e.g., Brodsky and Prejean, 2005).

Observational studies of triggering have made inferences about earthquake processes either by measuring a few observables (e.g., delay time) for large number of events (Velasco et al., 2008; Parsons and Velasco, 2011) or by measuring several observables from a limited number of events (e.g., Gomberg and Bodin, 1994; Hough and Kanamori, 2002; Wu et al., 2011). Our study is an example of the latter: a single, well-recorded triggered earthquake whose observations allow for the determination of its source mechanism, as well as its temporal relationship to the stress field of passing seismic waves. Here we report the occurrence of a M_w 3.9 strike-slip earthquake near Nenana, Alaska, that

* Corresponding author. Tel.: +1 907 474 5456.
E-mail address: carltape@gi.alaska.edu (C. Tape).

0012-821X
http://dx.doi.org/10.1016/j.epsl.2012.11.060

was triggered by Love waves from the M_w 8.6 offshore Sumatra earthquake. The 'Nenana' earthquake was preceded by a >24 s foreshock signal that exhibited exponential growth. We interpret this foreshock signal as a nucleation phase.

Laboratory experiments of nucleation (Dieterich and Kilgore, 1996; Ohnaka and Shen, 1999; Nielsen et al., 2010; Ben-David et al., 2010) and triggering (Savage and Marone, 2008), as well as theoretical models of nucleation (Dieterich, 1978; Lapusta and Rice, 2003; Rubin and Ampuero, 2005; Kaneko and Ampuero, 2011) and triggering (Gomberg et al., 1998; Perfettini et al., 2003), have explored how nucleation and subsequent ruptures are influenced by external forcing conditions. The Nenana earthquake provides the first observation of combined nucleation and triggering, and it suggests that transient stresses during nucleation can influence the subsequent earthquake rupture. We analyze the seismic observations in Sections 2 and 3. In Section 4 we pose three questions framing several possible scenarios. Our preferred interpretation is that the fault was unloaded with the arrival of the positive stress perturbation from the Sumatra Love wave. This initiated a slow, creep-like nucleation phase with exponential growth. The nucleation phase transitioned into a M_w 3.9 earthquake under a negative stress perturbation. Further theoretical and laboratory studies, as well as a search for nucleation phases in catalogs of triggered earthquakes, should help discriminate the interpretation scenarios for the Nenana earthquake.

1.1. Triggering terminology

Earthquakes produce static stresses due to elastic deformation, as well as dynamic stresses due to transient conditions from passing seismic waves. Both dynamic and static stresses can trigger smaller earthquakes (Freed, 2005). The relative importance of these effects can be quantified (Gomberg and Bodin, 1994; Gomberg et al., 1998; Belardinelli et al., 2003); in general terms, static stresses are dominant close to the mainshock event, whereas dynamic stresses are dominant in regions far from the mainshock event.

Remote triggering refers to dynamic triggering of events at distances where static stresses are minimal and dynamic stresses dominate. Based on an analysis of global seismicity following $M>7$ earthquakes, Parsons and Velasco (2011) identified a "mainshock region" of 1000 km for triggering large ($5<M<7$) earthquakes. Furthermore, they noted that the distance limit for triggering large earthquakes is "within $\sim 2-3$ mainshock rupture lengths". However, Pollitz et al. (2012) documented that $5.5 \le M \le 7$ earthquakes at remote distances can be triggered by the largest earthquakes ($M \ge 8.5$). Their findings suggest that there may be no magnitude limit for remotely triggered earthquakes, as previously suggested (Parsons and Velasco, 2011; Parsons et al., 2012).

Instantaneous triggering refers to the coincidence in time between the triggering stresses and the triggered event. Antonioli et al. (2006) defined instantaneous triggering to be when an event "occurs within the time interval during which the transient seismic signal is above the background noise level in that location". Instantaneous triggering can occur within the mainshock region (e.g., Antonioli et al., 2006) or beyond the mainshock region (e.g., Gomberg et al., 2004). However, by this definition the time interval of instantaneous triggering for the 2012 Sumatra event is approximately 5000 s (1.4 h) in Alaska (Table 1). Other studies have taken a more conservative view of "instantaneous". For example, using bin widths of 300 s, Velasco et al. (2008) analyzed delay times between the onset of passing Love waves and the origin time of triggered earthquakes. Other studies have identified delay times on the order of tens of seconds by showing the coincidence between cycles of the perturbing wave and the triggered earthquakes (e.g., West et al., 2005). The high-quality observations in our study allow us to interpret the events on a time scale on the order of seconds.

Our study documents a triggered earthquake that contains two parts: (1) a foreshock signal, interpreted as a nucleation phase and (2) a M_w 3.9 event, which we refer to as the mainshock. The triggered earthquake is unequivocally remote and instantaneous. The distance between the triggered event and the Sumatra event is 11,000 km, which is 37 times the source dimension of ~ 300 km inferred from finite slip models (Meng et al., 2012). The triggered sequence of nucleation phase and mainshock occurred within a single cycle of the dominant 130-s period Sumatra Love wave.

2. The Sumatra earthquake in Alaska

The April 11, 2012, offshore Sumatra earthquake (Meng et al., 2012) generated one of the largest global Love waves ever recorded. The large Love waves resulted from a combination of the magnitude (M_w 8.6), the shallow depth, and the near horizontal slip vector associated with the predominantly strike slip mechanism (Fig. 1a). The Love waves were particularly strong in Alaska, which was in the direction of maximal radiation and along a path that was purely continental and therefore less attenuating, relative to oceanic paths or mixed continental-ocean

Table 1
Key times and durations in this study. Station MDM is the closest station (32 km) to the triggered Nenana earthquake. By "at Nenana", we mean at the epicenter of the Nenana earthquake. For estimated times at Nenana we use the observed arrival time on MDM and apply an appropriate time shift. This time shift depends on the seismic phase of interest (P, Love, Rayleigh), the bandpass filter for the phase, and the earthquake generating the phase (Nenana or Sumatra). The Sumatra origin time is the PDE origin time listed in the GCMT catalog (www.globalcmt.org).

i	Event	t_i, UTC 11-April-2012	$t_i - t_2$ (s)	$t_i - t_7$ (s)
1	Sumatra origin time	08:38:37	−830.1	−2600.1
2	Start Sumatra P wave at Nenana	08:52:27	0.0	−1770.0
3	Qualitative end Sumatra P wave at Nenana	09:00:18	471.1	−1298.9
4	Sumatra Love wave positive shear strain at Nenana	09:20:44	1697.1	−72.9
5	Nenana foreshock signal rises above noise level	09:21:33	1746.0	−24.0
6	Sumatra Love wave max. negative shear strain ($T \ge 120$ s) at Nenana	09:21:50	1763.5	−6.5
7	Nenana mainshock origin time	09:21:57	1770.0	0.0
8	Sumatra Love wave max. negative shear strain at Nenana	09:22:03	1776.1	6.1
9	Nenana P arrival at MDM	09:22:04	1777.3	7.3
10	Qualitative end of Nenana waveforms at MDM	09:22:27	1800.0	30.0
11	Sumatra Love wave max. positive shear strain at Nenana	09:22:56	1829.5	59.5
12	Sumatra Rayleigh wave arrival at Nenana	09:28:18	2150.9	380.9
13	Qualitative end of Sumatra wave train at Nenana	10:13:56	4888.9	3118.9

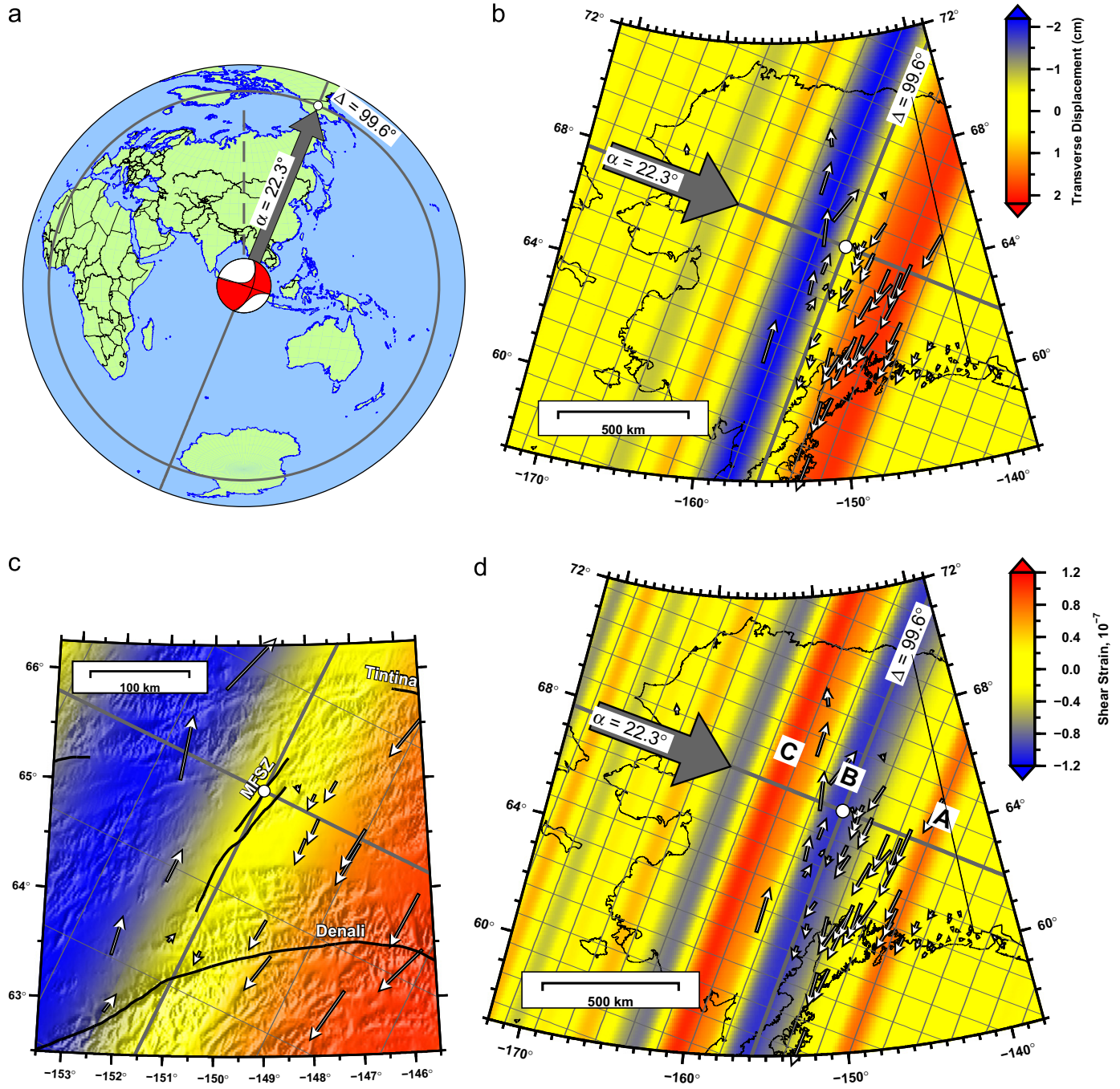

Fig. 1. Love waves in Alaska from the April 11, 2012 M_w 8.6 Sumatra earthquake. (a) Propagation path from Sumatra to central Alaska, at an azimuthal angle of $\alpha = 22.3^\circ$. The beachball symbol depicts the predominantly strike-slip rupture of the Sumatra earthquake (Dziewonski et al., 1981). (b) Horizontal displacement field in Alaska at the origin time of the M_w 3.9 Nenana earthquake in central Alaska. The epicenter of this event is marked by the white dot at the center of the thick gray lines. The large gray arrow denotes the wave propagation direction from Sumatra. The grid lines represent increments of 1° in α and 1° in Δ from the Nenana epicenter. (c) Expanded view of (b) in the region of the triggered event. Major active faults are labeled as Denali, Tintina, and MFSZ, the Minto Flats seismic zone. (d) Shear strain computed from the displacement field in (b).

paths (Dziewonski and Steim, 1982). By comparison, the M_w 9.2 2004 Sumatra-Andaman thrust earthquake, whose seismic moment was eight times that of the 2012 earthquake, generated Love wave amplitudes in Alaska that were half as large.

The ground motion in Alaska from the Sumatra earthquake was dominated by Love waves, with peak-to-peak amplitudes exceeding 4 cm (Tape, 2012). The dominant pulse was consistent in terms of its amplitude, its period content (100–160 s), and its velocity within Alaska (4.5 km/s; Fig. S1); the corresponding wavelength was approximately 580 km. Normal-mode synthetic seismograms for a radially symmetric (1D) Earth model and a point-source representation contain the basic features present in the seismograms in Alaska: a long-wavelength, cm-scale dominant Love wave followed by a Rayleigh wave 400 s later (Tromp et al., 2010). Rupture complexity or structural complexity need not be invoked to explain the dominant Love wave pulse that is central to this study.

We used the long-period Love wave to estimate a time-dependant displacement field across Alaska (Fig. 1b). We time-shifted all the Love wave recordings using the 4.5 km/s velocity,

then stacked the waveforms to obtain a single time series representative of the dominant transverse displacement across Alaska (Fig. S1). The constant velocity can then be used to transform the displacement seismogram into a time-dependent spatial wavefield. By selecting a particular time, we can plot an estimated snapshot of the transverse displacement field. Fig. 1b shows the observed horizontal vector field superimposed on the estimated transverse displacement field, plotted at the origin time of the M_w 3.9 Nenana earthquake. At this moment in time, the region of Alaska to the northwest of the Nenana epicenter was displaced by more than 2 cm to the northeast, and the region to the southeast of Nenana was displaced by approximately 2 cm to the southwest.

The estimated wavefield associated with the Love wave can be used to directly compute a strain tensor field (Appendix A and Fig. 1d). The corresponding Love wave from Sumatra exhibited three shear strain pulses (A, B, C in Fig. 1d), the middle of which was negative in sign and coincided with the triggered Nenana earthquake. The strain associated with each pulse was 0.79×10^{-7} (A), -1.0×10^{-7} (B), and 1.0×10^{-7} (C).

3. The Nenana earthquake

At 09:21:57 UTC the M_w 3.9 Nenana earthquake occurred within the Minto Flats seismic zone in central Alaska (Fig. 1c). The P wave from Sumatra had arrived 29.5 min earlier, the peak Love wave displacement occurred 53.6 s previously, and the zero displacement between Love wave peaks occurred 3.6 s previously (Fig. 2c and Table 1). The Nenana earthquake and its nucleation phase occurred within the duration of the 130 s period Sumatra Love wave and therefore constitute instantaneous triggering. A physical connection between the Love wave and triggered earthquake is likely, considering that a M_w 3.9 is expected to occur once every 3 yr in this seismic zone and once every 13 yr on this particular fault. (We determined these rates from frequency-magnitude distributions of earthquakes within the fault zone.)

The closest station to the Nenana earthquake was MDM (Murphy Dome), at 32 km (Fig. 2). Filtering the MDM seismogram at high frequencies reveals the Nenana earthquake (Fig. 2b). By time-shifting and stacking seismograms from nearby stations, we are able to determine the relative timing between the Sumatra Love waves and the Nenana triggered earthquake. The Nenana earthquake occurred almost exactly between the maximal displacement peaks of the Love wave (Figs. 1c and 2c), and coincident with the maximally negative strain (Figs. 1d and 2d).

The Nenana earthquake provides a rare opportunity to derive a robust source mechanism for an instantaneously triggered earthquake. For the Nenana earthquake, periods above 4 s are dominated by the Sumatra waves, especially on the vertical and radial components. We were able to obtain a high-quality focal mechanism for the event by fitting full-length waveforms filtered between 0.3 and 0.6 Hz. The full waveforms on all three components at the closest six stations were well fit by our synthetic seismograms (Fig. 3). An additional eight stations had high enough signal-to-noise for the (Nenana) Love waves to be fit as well. A grid search revealed a depth of 19 km, near the base of the relatively thin (25 km) crust in the region (Veenstra et al., 2006) (Fig. S3b).

The Nenana focal mechanism indicates strike-slip faulting on the western fault of the Minto Flats seismic zone (Fig. 4). The Minto Flats seismic zone accommodates left-lateral faulting

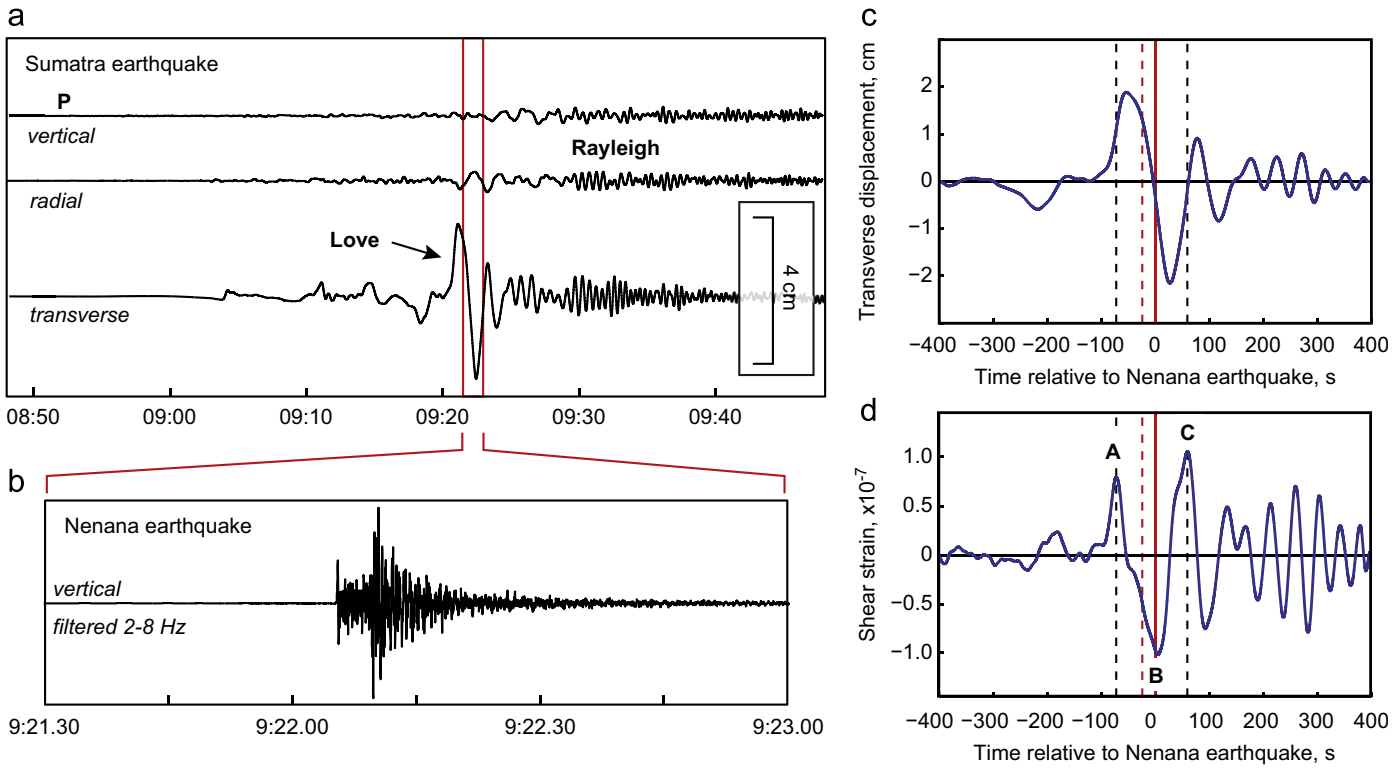

Fig. 2. The occurrence of the M_w 3.9 earthquake near Nenana, Alaska, coincident in time and space with 4 cm horizontal displacement Love wave from the Sumatra earthquake. (a) Representative three-component ground motion of the Sumatra earthquake in Alaska. This recording at MDM is the closest station (32 km) to the triggered Nenana earthquake. The Love wave is the dominant waveform throughout Alaska. (b) High-frequency filtered version of the same seismogram in (a) showing the M_w 3.9 Nenana earthquake. (c–d) Transverse displacement (c) and corresponding shear strain (d) at the Nenana epicenter, computed by stacking waveforms from the 13 closest stations (Fig. S1). The dashed black lines denote the positive shear strain pulses A and C (Fig. 1d). The dashed red line denotes the emergence of the foreshock signal from the noise at $t = -24$ s (Fig. 6).

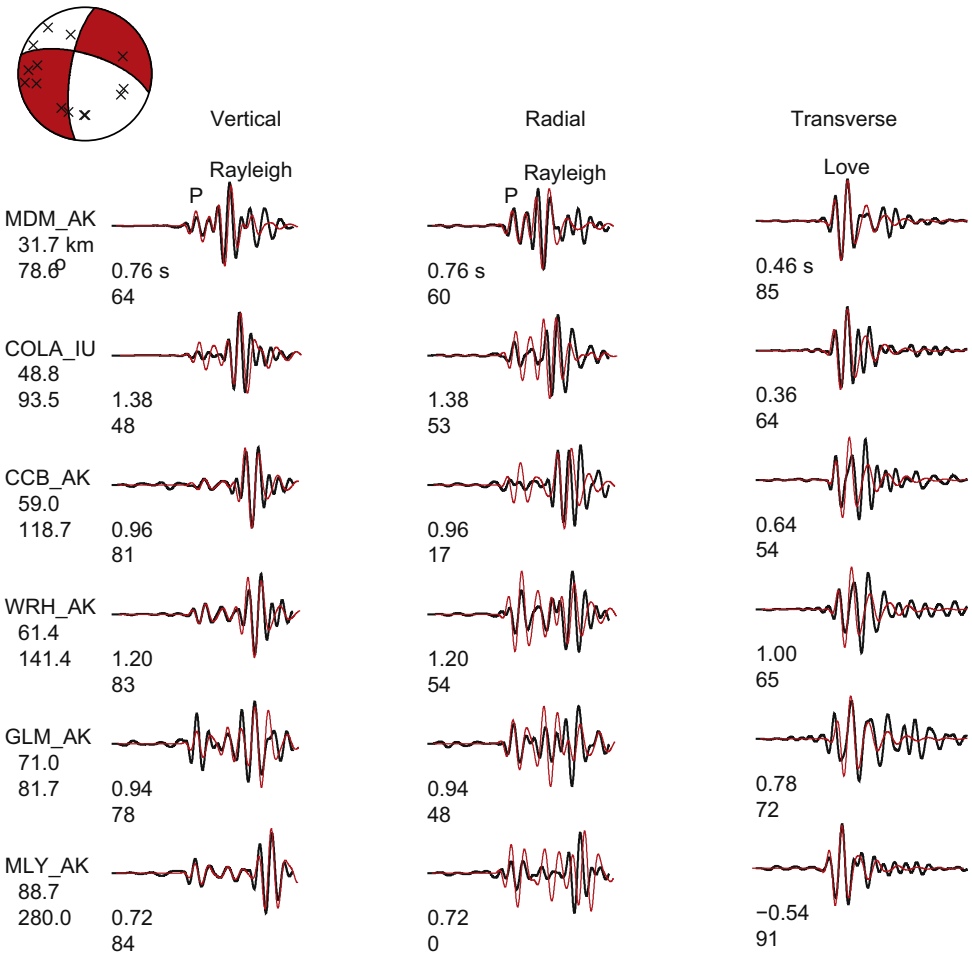

Fig. 3. Source inversion for the Nenana earthquake, using the method of Zhu and Helmberger (1996). Subset of observed three-component seismograms (black) compared with synthetic seismograms (red), both filtered between 0.3 Hz and 0.6 Hz. Stations are ordered in increasing distance from the source. Synthetic seismograms are computed using a frequency-wavenumber method Zhu and Rivera (2002). Synthetic seismograms are time-shifted for maximal cross-correlation, which accounts for (some) unknown 3D structure (Fig. S3a). The labels for each row list the azimuth of the station (relative to source) and the distance (to source). Below each seismogram pair are labels for the time shift required for maximum cross correlation (top), as well as the maximum cross correlation. See Fig. S2 for a complete display of all stations used in the inversion.

within a broad shear zone between the right-lateral faults of the Denali and Tintina–Kaltag system (Fig. 1b) (Page et al., 1995). Regional GPS measurements indicate minimal strain across the region (Freymueller et al., 2008), but seismicity reveals a concentration of consistent left-lateral deformation. The fault zone produced a M_w 6.0 in 1995 to the north of the Nenana event (Fig. 4) and a M_w 5.8 in 2000 to the south. These larger events, and the prevalence of similar focal mechanisms from smaller events (Ratchkovski and Hansen, 2002), allow us to infer a southwest-northeast fault plane for the Nenana earthquake. This is in agreement with the orientation of the western strand of the Minto Flats seismic zone (Fig. S4).

At 09:21:57, at the Nenana epicenter, we have good estimates for both the strain field and the radiation pattern of the triggered earthquake. The estimated Sumatra Love wave displacement field is perpendicular to the great circle path and approximately parallel to the strike-slip fault (Fig. 4). The fault is therefore nearly optimally oriented to slip under positive stresses imparted by Love waves from Sumatra. The principal axes of the Nenana earthquake are in agreement with fault slip in a direction comparable to the Sumatra Love wave displacement direction. The principal axes of the strain tensor associated with the Sumatra Love waves – at the Nenana origin time – differ from the horizontally projected principal axes of the Nenana earthquake by 13° and a change of sign (Fig. 4).

The Love wave can be used to estimate the stress perturbation at the origin time. The shear strain from the Sumatra Love wave at the Nenana epicenter is $s = -1.0 \times 10^{-7}$, with the negative sign representing right-lateral motion across a northeast-striking fault. Given the depth sensitivity of the $\sim$500 km Love wave, the strain at the hypocenter is nearly the same as at the surface. Our layered model used for synthetic seismogram modeling has a rigidity of $\mu = 35.2$ GPa at the hypocentral depth of 19 km. The shear stress perturbation due to the Sumatra Love wave at the Nenana hypocenter and origin time is

$$\sigma = 2\,\mu\,s = -6.8 \text{ kPa}, \tag{1}$$

where s is the shear strain (Eq. (A.3)).

We can estimate the approximate size of the fault using the relationship between seismic moment and stress drop for a circular fault (Shearer, 2009). The seismic moment for the Nenana earthquake was 8.1×10^{14} N m. We were unable to obtain reliable stress drop estimates for the earthquake, but if we assume "end member" stress drops of 0.2 MPa and 20 MPa (Shearer et al., 2006), then the corresponding fault radius is 1.21 km and 0.26 km.

The Nenana earthquake was preceded by an intriguing foreshock signal originating from the same location. A high-frequency filtered record section of velocity seismograms shows a characteristic decrease in amplitude with distance from the Nenana epicenter (Fig. 5). At 16.4 s before the mainshock there is a

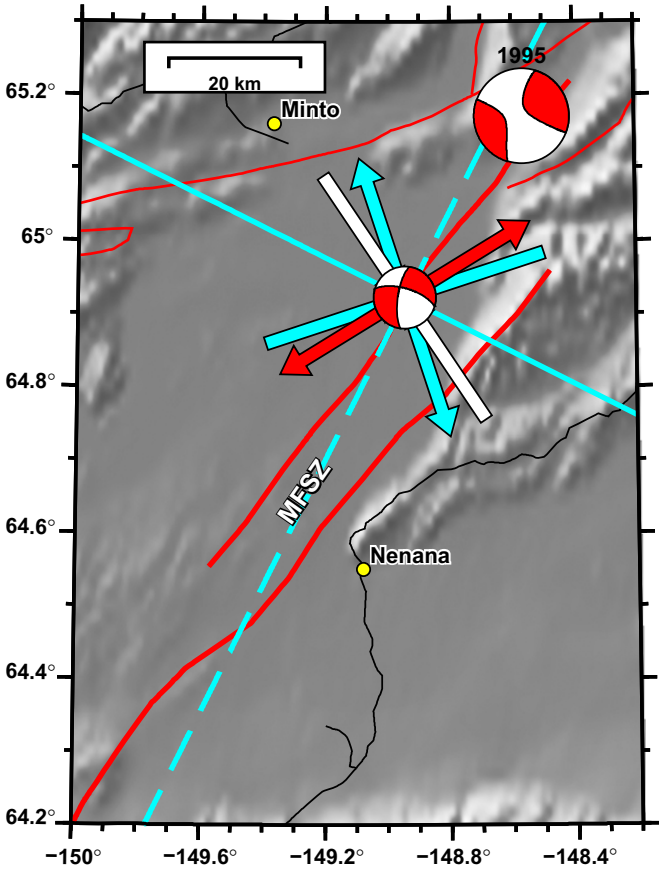

Fig. 4. Earthquake source mechanism for the 2012-04-11 M_w 3.9 Nenana earthquake in comparison with the orientation of Sumatra Love waves. The comparison is made at the Nenana earthquake epicenter at the origin time of the Nenana earthquake. The Sumatra Love waves propagate along the great-circle path from Sumatra (solid cyan line) and impart horizontal ground motion in the perpendicular direction (dashed cyan line). The principal axes of the associated strain tensor are shown as cyan arrows. The principal axes for the Nenana source mechanism are plotted as red arrows and white arrows. Inward-pointing arrowheads for *P*-axis directions are hidden beneath the beachball. The 1995-10-06 M_w 6.0 earthquake source mechanism is plotted for comparison. Both earthquakes are consistent with left-lateral strike slip fault motion on the western of the two faults comprising the Minto Flats seismic zone (MFSZ; Fig. S4).

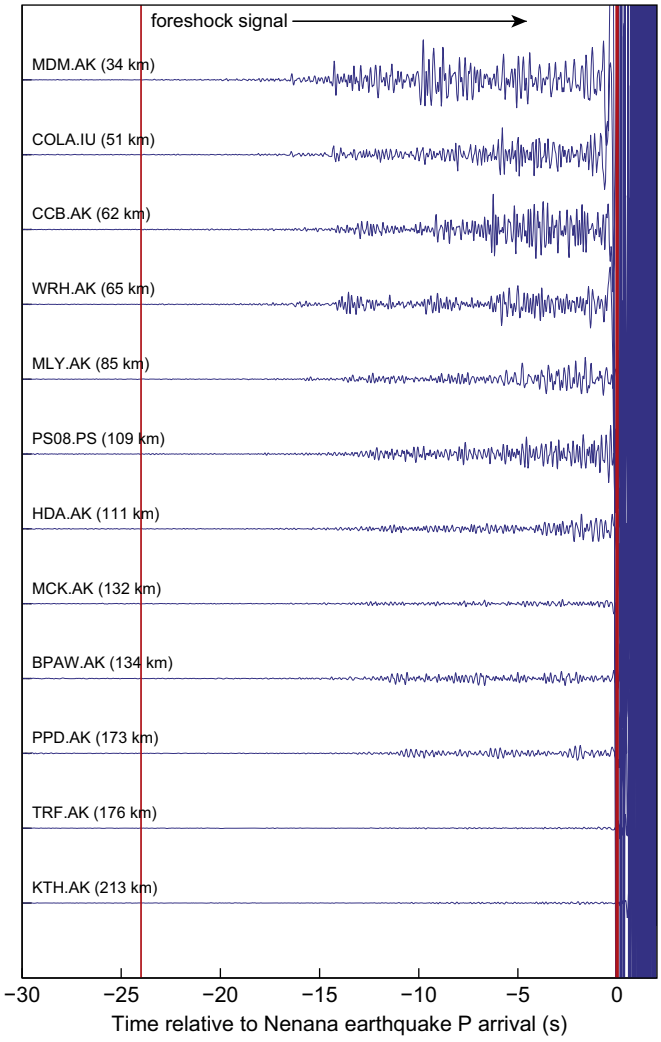

Fig. 5. Record section of the 24 s foreshock signal prior to the Nenana earthquake. The seismograms are the vertical component of velocity, filtered 2–8 Hz, ordered by distance from the Nenana epicenter, and aligned on the P onset of the mainshock. The vertical line at −24 s is the time at which the foreshock signal rises above the pre-Sumatra background noise level, as shown in Fig. 6. At time −16.4 s is the first visible pulse that is present on multiple stations. The alignment of this pulse, in addition to the decrease in amplitude with distance, indicate that the foreshock signal is in the same region as the mainshock.

coherent pulse visible at multiple stations. The tremor-like signal grows in amplitude and then abruptly transitions into the mainshock P waveform. The foreshock signal is best viewed in a log-scaled plot of the envelope of the seismograms (Fig. 6), which reveals three important time intervals: background noise, the foreshock signal, and the mainshock. The seismograms reveal a start time of the foreshock signal that is at least 24 s before the mainshock.

The amplitude of the foreshock signal grows exponentially over the 24 s period. The exponential growth can be expressed as

$$A(t) = A_0 e^{m(t-t_P)}, \quad t < t_P, \tag{2}$$

where t_P is the P onset of the mainshock, $A_0 = A(t_P)$ is the amplitude of the signal just before the P arrival, and m is the slope in log space that describes the growth of the foreshock signal. For the two stations in Fig. 6, we obtain m values of 0.22 s^{-1} and 0.21 s^{-1}. All ten other stations analyzed (Fig. 5) exhibited a foreshock signal with exponential growth. For more distant stations, the signal is weaker, as expected, and therefore the time at which the foreshock signal rises above the noise is later.

The decay of the foreshock signal with distance from the Nenana epicenter (Fig. 5) can be used to obtain a rough estimate for the location of the foreshock signal. We performed a grid search for possible source locations, while fitting a linear model to the values of $\log A_0$ (Fig. S5). This analysis assumes that attenuation of the signal is constant everywhere, which is unlikely in such a region with a large sedimentary basin (Van Kooten, 2012), crustal variations (Veenstra et al., 2006), and complex upper mantle heterogeneities (Rondenay et al., 2010). Nevertheless, we are able to use the amplitude variations of the foreshock signal to show that the Nenana epicenter is a plausible source location (Fig. S5). We did not identify unequivocal, locatable sub-events within the foreshock signal.

3.1. One event versus two events

A fundamental question is whether the foreshock signal in Fig. 6 occurs at or near the Nenana hypocenter, or whether it is a

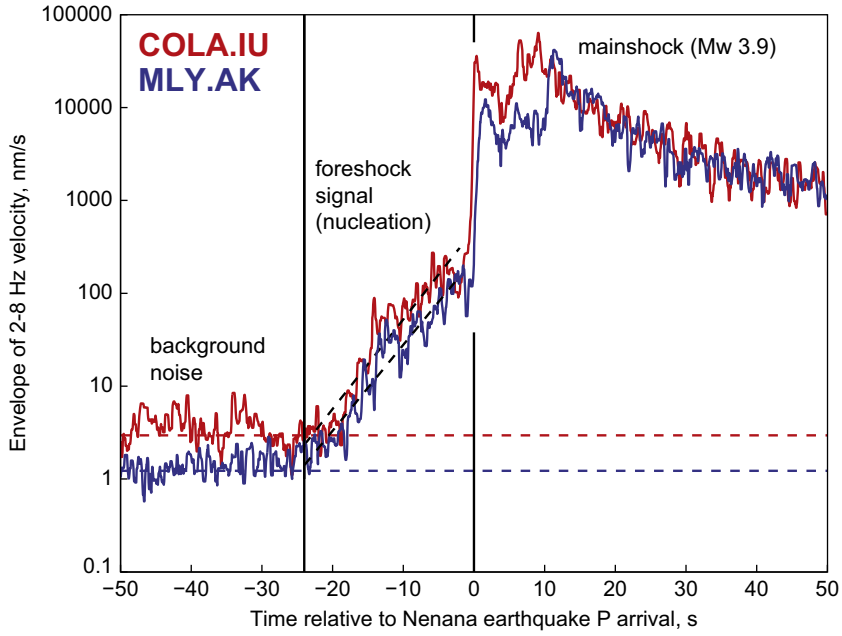

Fig. 6. Envelope of velocity seismograms for two representative stations. The amplitudes are plotted on a log scale so that the noise level, foreshock signal, and mainshock are all visible. The linear slope of the foreshock signal represents an exponential growth in amplitude. MLY.AK is 86 km northwest of the Nenana epicenter; COLA.IU is 51 km east of the Nenana epicenter.

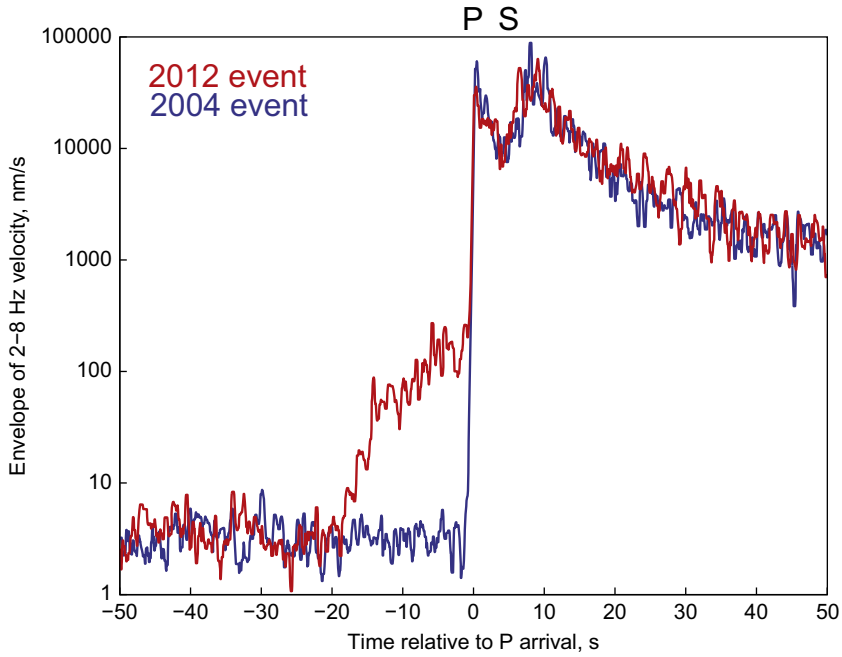

Fig. 7. Comparison between the 2012-04-11 M_w 3.9 and 2004-11-17 M_w 3.6 earthquakes, recorded at COLA.IU. The 2004 event has similar hypocenter, magnitude, and source mechanism to the 2012 event. The striking difference between these two records is the 2012 foreshock signal, interpreted as a nucleation phase.

separate process occurring in a separate place. The preceding attenuation analysis shows that the foreshock signal must be within 20 km or so of the Nenana epicenter. Next we examine the temporal variation, considering the possibility of two simultaneous signals. Fig. 7 compares the high-frequency envelope of seismograms recorded at COLA.IU for the 2012 Nenana earthquake and for a 2004 comparison event with similar source parameters (Table S1). The two time series show striking similarity in their amplitudes for the earthquakes ($t > 0$). (Note that no amplitude scaling has been applied.) The foreshock signal in the 2012 event is the obvious difference, and the comparison shows that the foreshock signal could not have continued on the same linear trajectory for more than 20 s after the mainshock; otherwise we would see it manifested within the earthquake coda of the 2012 event. The comparison suggests that the foreshock signal 'stopped' close in time to the mainshock initiation. The most plausible explanation is that there was one event in the same location, with the foreshock signal 'becoming' the mainshock signal. Our subsequent interpretation is based on the one-event model.

4. Interpretation

The foreshock signal indicates that the Nenana earthquake nucleated as a slow creep-like process at least 24 s before the mainshock. Two aspects of the Nenana earthquake need explanation: the exponential growth of the foreshock signal (Fig. 6) and the coincidence of the M_w 3.9 mainshock with the peak negative stress perturbation (Fig. 2d). Observations alone cannot discriminate among several possible interpretations. Below we outline three key questions, which frame eight possible scenarios. Further evidence from additional observations and from theoretical and laboratory studies may help discriminate among the different scenarios for the Nenana earthquake.

4.1. Key questions

We pose three questions associated with three time periods: (1) the time before the nucleation phase, (2) the time during which the nucleation phase is visible, and (3) the time of triggering of the M_w 3.9 mainshock. Fig. 8 serves as a guide to these time intervals.

There are eight possible scenarios, each of which is some combination of the letters E/F, I/J, and R/S (Fig. 8). After posing the key questions, we discuss three scenarios: FIR, FIS, and EIS.

4.1.1. When did nucleation start? (E or F)

The nucleation phase was underway at least 24 s before the M_w 3.9 event was triggered. Prior to −24 s we can only speculate what occurred. In Fig. 8 we suggest two possibilities, labeled E and F. With E, the nucleation phase begins just before −24 s. The starting point for path E is unknown, since we do not know the size of the first asperity that slipped. The nucleation could have started earlier, as suggested by path F. We propose path F based on the timing of the peak positive stress perturbation from the Sumatra Love waves, at −72.9 s. We show two possible paths for how nucleation proceeded. Exponential nucleation growth could have started at the outset (F1) or at some time later (F2).

If nucleation started at −72.9 s, then the principal axes of the Love wave stress field are quite similar to the principal axes of the triggered earthquake. Using the time of −72.9 s instead of 0 s, when stresses were negative, would have the effect of flipping the directions of the Sumatra strain axes in Fig. 4. In this case, the 3D rotation angle between the two sets of principal axes would be $\xi_0 = 34^\circ$, which is statistically small (e.g., Fig. 11. of Tape and Tape, 2012).

4.1.2. Was exponential nucleation growth influenced by the Sumatra stresses? (I or J)

The exponential growth in nucleation occurred during the time-varying stress perturbation of the Sumatra Love wave (Fig. 2d). However, we cannot determine if the Sumatra stresses influenced

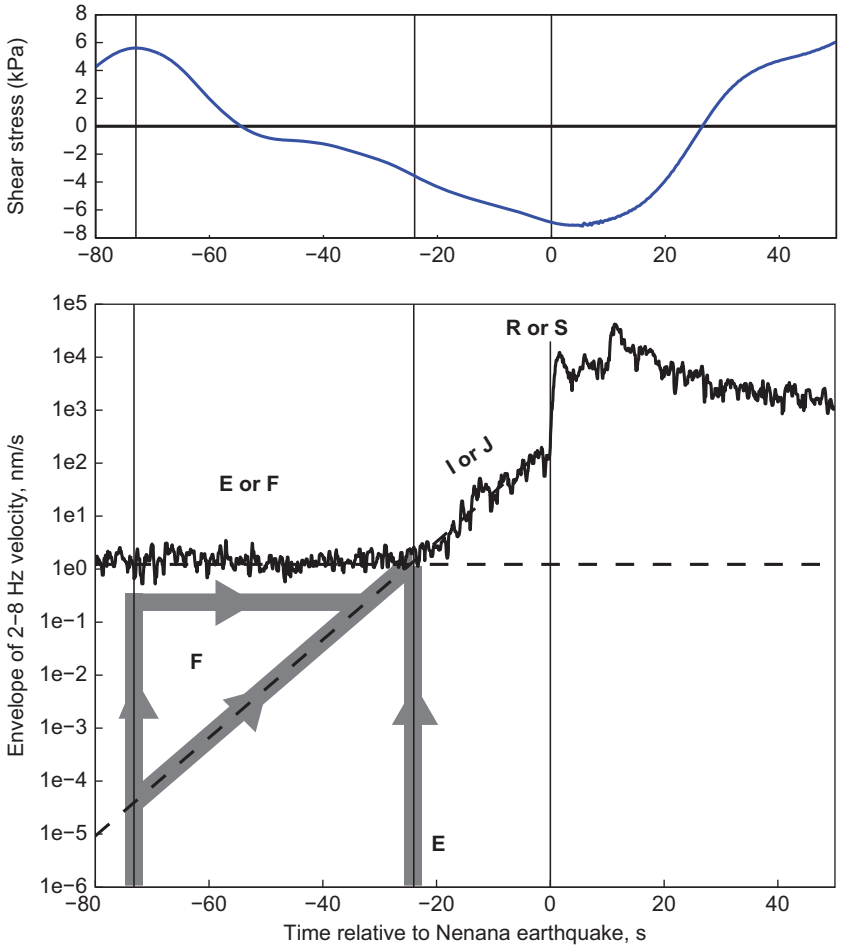

Fig. 8. Guide to interpretation scenarios for the Nenana earthquake (Section 4). (Bottom) The example time series is the MLY record in Fig. 6. The vertical line at $t = -72.9$ s is the peak positive shear stress perturbation from the Sumatra Love wave. (Top) Shear stress perturbation due to the Sumatra Love waves (Eq. A.3), in kilopascals. This is the shear strain time series in Fig. 2d, scaled to shear stress.

the exponential growth (case J), or not (case I). In the three example scenarios below we have assumed case I, in part because there is no direct correlation between the time variations of the Sumatra stresses and the (constant) signal of the nucleation phase. Furthermore, exponential nucleation has been predicted from theoretical models of slip-dependent friction (e.g., Campillo and Ionescu, 1997; Ampuero et al., 2002).

4.1.3. What caused the M_w 3.9 mainshock? (R or S)

We propose two possibilities for the occurrence of the mainshock, labeled R or S. With case R, the mainshock triggering is not influenced by stresses from the passing Sumatra Love waves; with case S, it is.

4.2. Scenario FIR: nucleation occurs during positive stress perturbation; triggering unrelated to stress

The Nenana earthquake occurred under shear stress perturbations of $|\sigma| \sim 5$ kPa from the Sumatra Love wave. These perturbations are small relative to the range of typical stresses of 20–40 MPa on strike-slip faults (Brune and Thatcher, 2002). Therefore we infer that the fault was critically loaded and near failure.

Because we have the unusual circumstance of having the source mechanism of the triggered earthquake, we must also reconcile the sign of the perturbation stress with the stresses implied from the triggered earthquake. The left-lateral strike-slip mechanism of the Nenana earthquake is consistent with the predominant mode of faulting in the region (Fig. 4). If this fault had been critically loaded, then a positive shear stress perturbation would have been most likely to unload the fault. A negative stress perturbation would have lessened the loading and therefore impeded triggering. Thus, case F places the onset of nucleation at the peak of the positive stress perturbation from Sumatra (Fig. 8).

In scenario FIR, the Sumatra Love wave unloads the fault at -72.9 s, and there is no further connection between the Sumatra Love wave and the sequence of events. That is, the ensuing slow nucleation and mainshock triggering would have occurred anyway. (Unfortunately, we cannot repeat this experiment.) A slow-slipping, growing patch on the fault could expand in both area and slip, resulting in a cascading of microearthquakes and an exponential growth in moment. This might be related to foreshock acceleration observed in non-triggered settings (Peng et al., 2007; Bouchon et al., 2011). The rapid acceleration from the foreshock signal to the mainshock could occur without any external transient stress perturbations, as demonstrated in laboratory and theoretical studies (Dieterich, 1978; Lapusta and Rice, 2003; Kaneko and Ampuero, 2011), and suggested from observations of earthquakes triggered by creep events (Peng and Gomberg, 2010; Shelly et al., 2011).

4.3. Scenario FIS: nucleation and triggering both caused by stress perturbation

Our preferred scenario differs from the previous scenario only in the interpretation of the mainshock triggering (R versus S). Our preferred interpretation posits that the mainshock occurrence at peak negative stress (Fig. 1) was not a coincidence. The dominant long-length-scale peak negative shear stress occurred during the growing foreshock signal and ~ 6 s before the Nenana mainshock (Table 1). We speculate that the mainshock occurred at the time when the resisting shear stresses started to diminish. Thus the Love wave strain pulse A in Fig. 2d nucleated the earthquake, and pulse B triggered the mainshock, 73 s later (Table 1).

4.4. Scenario EIS: nucleation and triggering occur during negative stress perturbation

From a purely observational standpoint, the simplest explanation is that the nucleation phase started "close" in time to when the signal exceeded the noise level, at -24 s, labeled as E in Fig. 8. This interpretation requires the least extrapolation of the nucleation phase to earlier times. The mainshock coincided with peak negative stresses, as in scenario FIS. The key distinction from FIS is that with EIS we have no physical mechanism for how the fault could be unloaded under negative shear stresses. Nevertheless, it is possible that other factors could be significant, such as normal stresses or the prolonged shaking and stressing of the entire fault zone.

5. Discussion and conclusion

The Love wave from the 2012-04-11 M_w 8.6 offshore Sumatra earthquake triggered a M_w 3.9 strike-slip earthquake in central Alaska that was preceded by a slow, creep-like nucleation phase with exponential growth. The sequence of events, including the nucleation phase, was well-recorded by 12 stations within 200 km of the epicenter near Nenana, Alaska. Despite the quality of the observations, it is impossible to isolate the physical processes responsible for the observations, at least from observations alone. In Section 4 we use three questions to frame the different interpretation scenarios.

The nucleation phase of the Nenana earthquake is a rare observational example of earthquake nucleation. The closest analog to the Nenana earthquake foreshock signal is the foreshock signal of the 1999 M_w 7.6 Izmit earthquake. Using a single discontinuous seismogram, Bouchon et al. (2011) identified a 44-min long nucleation phase comprised of several repeating, nearly identical waveforms. The four largest Izmit foreshocks occur at 43 min (4th), 20 min (3rd), 12 min (2nd), and 2 min (1st) before the mainshock, indicating an acceleration and growth of the largest foreshocks. The Nenana foreshock signal (Fig. 5) may represent a sequence of many microearthquakes in the Nenana hypocentral region, but, unlike the Izmit foreshock sequence, the events are not separated in time enough to attribute all the waveforms to distinct events. The amplitude growth of the foreshock signal is better quantified in the case of Nenana than in the case of Izmit (Section 3). All 12 stations for the Nenana earthquake exhibit exponential growth during nucleation (Eq. (2)), whereas with Izmit the growth is somewhat qualitative.

A second connection between the Izmit and Nenana nucleation phases is in their comparably deep hypocenters. The Izmit hypocenter was at a depth of 15 ± 2 km (Bouchon et al., 2011), near the base of the 17 km crust (Özalaybey et al., 2002). The Nenana hypocenter was at a depth of 19 ± 1 km (Supplementary Fig. S3b), also near the base of the 25 km crust (Veenstra et al., 2006). Bouchon et al. (2011) attributed the Izmit nucleation phase to fault creep in the area surrounding a patch that repeatedly failed and that ultimately started the M_w 7.6 earthquake. We, too, attribute the Nenana nucleation phase to fault creep. However, we do not have evidence that the same patch is repeatedly failing. Therefore we prefer an interpretation in which the creep patch is growing radially, with the foreshock signal manifested by tiny asperities breaking at the boundary of the growing patch. This patch eventually breaks a much larger asperity associated with the M_w 3.9 mainshock. In Section 4 we speculate as to whether this process was influenced by the dynamic stresses from Sumatra.

Shelly et al. (2011) demonstrated that seismic waves from large events can trigger slow creep events at depths of 20–30 km

on the San Andreas fault. These triggered creep events can be thought of as a collection of repeating microearthquakes that migrate at rates of tens of meters per second over a time period of hours to days. Shelly et al. (2011) acknowledged that a creep event could possibly trigger earthquakes secondarily; in other words, seismic waves from distant earthquakes trigger a slow creep event, which in turn can trigger earthquakes in the immediate vicinity. In the case of the Nenana sequence, we see that the nucleation phase (or 'creep event') led directly into the M_w 3.9 mainshock (Fig. 6). However, as discussed in Section 4, this might be better thought of as a natural progression of nucleation from a slow stage to rapid slip, rather than as a creep-like nucleation event that triggers a larger earthquake. Regarding the exponential growth of the Nenana nucleation phase, it would be interesting to see whether any of the creep events in Shelly et al. (2011) exhibited growth in amplitude as the event evolved.

The 2012 M_w 8.6 offshore Sumatra earthquake triggered several large ($5.5 \le M_w \le 7$) earthquakes. These earthquakes were preferentially strike-slip mechanisms and within the maximal radiation region of the Sumatra Love waves (Pollitz et al., 2012). Some of the events occurred during the passage of the Sumatra waves, while others occurred days later. The key point is that the M_w 8.6 earthquake elevated the global seismicity rate of $M_w \ge 5.5$ earthquakes. However, with the larger delay times it is challenging to determine exactly which earthquakes were triggered and which earthquakes would have occurred anyway, in the absence of the Sumatra earthquake. The Nenana earthquake was also strike-slip and favorably oriented for large dynamic shear stresses from Sumatra (Fig. 1a). What is special about the Nenana earthquake is that it was instantaneously triggered and it exhibited a tremor-like nucleation phase. It remains to be seen whether a nucleation phase is associated with other triggered events, such as those in Pollitz et al. (2012) or Velasco et al. (2008), or whether there is something particularly special about the crustal setting near Nenana, Alaska. If it is the latter, then seismic stations will be needed in the Minto Flats seismic zone (there are none), in order to detect any tremor-like signals and to better characterize the fault structure.

The Nenana earthquake raises hypotheses that can be tested with numerical models, laboratory experiments, and earthquake observations. The first question is whether exponential growth of a nucleation phase requires a time-varying stress perturbation. Based on laboratory and theoretical studies (e.g., Campillo and Ionescu, 1997; Ampuero et al., 2002; Kaneko and Ampuero, 2011) and observations (Bouchon et al., 2011), it seems plausible that a time-varying stress perturbation is not required; however, in this case we would expect to find many more observational examples of exponential nucleation. The second question is whether a time-varying stress perturbation can accelerate a 'minor' event, such as the interpreted nucleation phase, into a mainshock, once a dynamic rupture is underway. Theoretical and laboratory studies have explored how various forcing parameters influence triggering (e.g., Gomberg et al., 1998; Perfettini et al., 2003; Savage and Marone, 2008). The Nenana earthquake poses a challenge to theoretical and laboratory studies to include the physics of nucleation and dynamic triggering within the same framework, and it motivates seismologists to reexamine remotely triggered earthquakes for the presence of a nucleation phase.

Acknowledgments

We used data from the Alaska Earthquake Information Center and from the IRIS Data Management Center. These data were produced from the following seismic networks (Table 1 of Tape, 2012): AK, CN, AV, XZ, AT, IU, US, TA, and II. The manuscript benefitted from comments from Yoshi Kaneko, Jeff Freymueller, and Silvio De Angelis, and from two reviewers (Michel Bouchon and anonymous). We acknowledge support from the National Science Foundation under Grant EAR-1215959.

Appendix A. Computing the strain wavefield

We consider a $\hat{\mathbf{r}}$-$\hat{\boldsymbol{\Delta}}$-$\boldsymbol{\alpha}'$ reference frame, where r is the radial (upward) coordinate, Δ is the arc distance from Sumatra, and $\alpha' = -\alpha$ is the azimuthal angle from Sumatra but in the opposite sense. The basis $\hat{\mathbf{r}}$-$\hat{\boldsymbol{\Delta}}$-$\boldsymbol{\alpha}'$ is right handed, $-\hat{\boldsymbol{\alpha}}'$ is the same direction as positive transverse component, and toroidal motion is therefore given by $\mathbf{u} = u_{\alpha'}\hat{\boldsymbol{\alpha}}' = -u_{\alpha}\hat{\boldsymbol{\alpha}}' = -u_{\mathrm{T}}\hat{\boldsymbol{\alpha}}'$.

The gradient of the displacement field, $\mathbf{L} = \boldsymbol{\nabla}\mathbf{u}$, is directly computed in Δ-α coordinates (with Sumatra at $\Delta = 0$ at the pole) The estimated strain tensor is the symmetric part of $\mathbf{L}$, $\boldsymbol{\varepsilon} = 0.5(\mathbf{L}+\mathbf{L}^T)$. Considering the dominant Love waveform in this study (Fig. 2), we can approximate the wavefield in Alaska by pure toroidal motion. We neglect changes in the vertical direction that are associated with the depth variations of the toroidal displacement eigenfunction, and we neglect changes in the transverse direction that are associated with the Sumatra source radiation pattern. The time-dependent symmetric strain tensor (Malvern, 1969) then reduces to

$$\boldsymbol{\varepsilon}(r,\Delta,\alpha') = -\begin{bmatrix} 0 & 0 & \frac{1}{2r}(u_{\alpha'}) \\ 0 & 0 & \frac{1}{2r}\left(u_{\alpha'}\cot\Delta - \frac{\partial u_{\alpha'}}{\partial\Delta}\right) \\ \epsilon_{r\alpha'} & \epsilon_{\Delta\alpha'} & 0 \end{bmatrix} \tag{A.1}$$

$$\boldsymbol{\varepsilon}(r,\Delta,\alpha') = \begin{bmatrix} 0 & 0 & \frac{1}{2r}(u_{\mathrm{T}}) \\ 0 & 0 & \frac{1}{2r}\left(u_{\mathrm{T}}\cot\Delta - \frac{\partial u_{\mathrm{T}}}{\partial\Delta}\right) \\ \epsilon_{r\alpha'} & \epsilon_{\Delta\alpha'} & 0 \end{bmatrix}, \tag{A.2}$$

where $u_{\mathrm{T}} = -u_{\alpha'}$.

The shear strain term, with explicit dependence on Δ and t and evaluated at the Earth's surface ($r = R$), is

$$s(\Delta,t) \equiv \epsilon_{\Delta\alpha'}(\Delta,t) = \frac{1}{2R}\left(u_{\mathrm{T}}(\Delta,t)\cot\Delta - \frac{\partial u_{\mathrm{T}}}{\partial\Delta}(\Delta,t)\right). \tag{A.3}$$

The magnitude of shear strain, $|s|$, will differ from the matrix norm of the strain tensor, $\|\boldsymbol{\varepsilon}\| = (\boldsymbol{\varepsilon}:\boldsymbol{\varepsilon})^{1/2}$. In our case, $|u_{\mathrm{T}}| \approx 0.01\left|\partial u_{\mathrm{T}}/\partial\Delta\right|$, and we can neglect the non-derivative terms of u_{T}. In that case the strain tensor has only two non-zero entries, $\epsilon_{\Delta\alpha'}$ (represented by s), and the norm is $\|\boldsymbol{\varepsilon}\| = \sqrt{2s^2} = \sqrt{2}|s|$.

Appendix B. Supplementary material

Supplementary material associated with this article can be found in the online version at http://dx.doi.org.10.1016/j.epsl.2012.11.060.

References

Ampuero, J.-P., Vilotte, J.-P., Sánchez-Sesma, F.J., 2002. Nucleation of rupture under slip dependent friction law: Simple models of fault zone, J. Geophys. Res., 107(B12), 2324, http://dx.doi.org/10.1029/2001JB000452.

Antonioli, A., Belardinelli, M.E., Bizzarri, A., Vogfjord, K.S., 2006. Evidence of instantaneous dynamic triggering during the seismic sequence of year 2000 in south Iceland. J. Geophys. Res. 111, B03302, http://dx.doi.org/10.1029/2005JB003935.

Belardinelli, M.E., Bizzarri, A., Cocco, M., 2003. Earthquake triggering by static and dynamic stress changes. J. Geophys. Res. 108 (B3), 2135, http://dx.doi.org/10.1029/2002JB001779.
Ben-David, O., Cohen, G., Fineberg, J., 2010. The dynamics of the onset of frictional slip. Science 330, 211–214.
Beroza, G.C., Ellsworth, W.L., 1996. Properties of the seismic nucleation phase. Tectonophysics 261, 209–227.
Bouchon, M., Karabulut, H., Aktar, M., Özalaybey, S., Schmittbuhl, J., Bouin, M.P., 2011. Extended nucleation of the 1999 M_w 7.6 Izmit earthquake. Science 331, 877–880.
Brodsky, E.E., Prejean, S.G., 2005. New constraints on mechanisms of remotely triggered seismicity at Long Valley Caldera. J. Geophys. Res. 110, B04302, http://dx.doi.org/10.1029/2004JB003211.
Brune, J.N., Thatcher, W. 2002. Strength and energetics of active fault zones. In: Lee, W.H.K., Kanamori, H., Jennings, P.C., Kisslinger, C. (Eds.), International Handbook of Earthquake and Engineering Seismology, International Geophysics Series, vol. 81A, Academic Press, pp. 569–588.
Campillo, M., Ionescu, I.R., 1997. Initiaion of antiplane shear instability under slip dependent friction. J. Geophys. Res. 102 (B9), 20,363–20,371.
Dieterich, J.H., 1978. Preseismic fault slip and earthquake prediction. J. Geophys. Res. 83, 3940–3948.
Dieterich, J.H., Kilgore, B., 1996. Implications of fault constitutive properties for earthquake prediction. Proc. Natl. Acad. Sci. U.S.A. 93, 3787–3794.
Dziewonski, A., Chou, T.A., Woodhouse, J.H., 1981. Determination of earthquake source parameters from waveform data for studies of global and regional seismicity. J. Geophys. Res. 86, 2825–2852. GCMT catalog at 〈www.globalcmt.org〉.
Dziewonski, A.M., Steim, J.M., 1982. Dispersion and attenuation of mantle waves through waveform inversion. Geophys. J. R. Astron. Soc. 70, 503–527.
Ellsworth, W.L., Beroza, G.C., 1995. Seismic evidence for an earthquake nucleation phase. Science 268, 851–855.
Freed, A.M., 2005. Earthquake triggering by static, dynamic, and postseismic stress transfer. Annu. Rev. Earth Planet. Sci. 33, 335–367.
Freymueller, J.T., Woodard, H., Cohen, S.C., Cross, R., Elliott, J., Larsen, C.F., Hreinsdóttir, S., Zweck, C., 2008. Active deformation processes in Alaska, based on 15 years of GPS measurements. In: Freymueller, J.T., Haeussler, P.J., Wesson, R., Ekström, G. (Eds.), Active Tectonics and Seismic Potential of Alaska, vol. 179, Geophysical Monograph. American Geophysical Union, Washington, DC, pp. 1–42.
Gomberg, J., Beeler, N.M., Blanpied, M.L., Bodin, P., 1998. Earthquake triggering by transient and static deformations. J. Geophys. Res. 103, 24,411–24,426.
Gomberg, J., Bodin, P., 1994. Triggering of the M_s=5.4 Little Skull Mountain, Nevada, earthquake with dynamic strains. Bull. Seismol. Soc. Am. 84, 844–853.
Gomberg, J., Bodin, P., Dragert, H., 2004. Earthquake nucleation by transient deformations caused by the M=7.9 Denali, Alaska, earthquake. Nature 427, 621–624.
Hill, D.P., 2008. Dynamic stresses, Coulomb failure, and remote triggering. Bull. Seismol. Soc. Am. 98, 66–92.
Hill, D.P., et al., 1993. Seismicity remotely triggered by the magnitude 7.3 Landers, California, earthquake. Science 260, 1617–1623.
Hough, S.E., Kanamori, H., 2002. Source properties of earthquakes near the Salton Sea triggered by the 16 October 1999 *M*7.1 Hector Mine, California, earthquake. Bull. Seismol. Soc. Am. 92, 1281–1289.
Iio, Y., 1995. Observations of the slow initial phase generated by microearthquakes: Implications for earthquake nucleation and propagation. J. Geophys. Res. 100 (B8), 15,333–15,349.
Kaneko, Y., Ampuero, J.-P., 2011. A mechanism for preseismic steady rupture fronts observed in laboratory experiments. Geophys. Res. Lett. 38, L21307, http://dx.doi.org/10.1029/2011GL049953.
Lapusta, N., Rice, J.R., 2003. Nucleation and early seismic propagation of small and large events in a crustal earthquake model. J. Geophys. Res. 108 (B4), 2205, http://dx.doi.org/10.1029/2001JB000793.
Lockner, D.A., Morrow, C., Moore, D., Hickman, S., 2011. Low strength of deep San Andreas fault gouge from SAFOD core. Nature 472, 82–86.
Malvern, L.E., 1969. Introduction to the Mechanics of a Continuous Medium. Prentice-Hall, Upper Saddle River, NJ, USA.
Meng, L., Ampuero, J.-P., Stock, J., Duputel, Z., Luo, Y., Tsai, V.C., 2012. Earthquake in a maze: compressional rupture branching during the 2012 M_w 8.6 Sumatra Earthquake. Science 337, 724–726.
Miyazawa, M., Brodsky, E.E., 2008. Deep low-frequency tremor that correlates with passing surface waves. J. Geophys. Res. 113, B01307, http://dx.doi.org/10.1029/2006JB004890.
Mori, J., Kanamori, H., 1996. Initial rupture of earthquakes in the 1995 Ridgecrest, California sequence. Geophys. Res. Lett. 23, 2437–2440.
Nielsen, S., Taddeucci, J., Vinciguerra, S., 2010. Experimental observation of stick-slip instability fronts. Geophys. J. Int. 180, 697–702.
Ohnaka, M., Shen, L., 1999. Scaling of the shear rupture process from nucleation to dynamic propagation: implications of geometric irregularity of the rupturing surfaces. J. Geophys. Res. 104, 817–844.
Özalaybey, S., Ergin, M., Aktar, M., Tapirdamaz, C., Biçmen, F., Yörük, A., 2002. The 1999 İzmit earthquake sequence in Turkey: seismological and tectonic aspects. Bull. Seismol. Soc. Am. 92, 376–386.
Page, R.A., Plafker, G., Pulpan, H., 1995. Block rotation in east-central Alaska: a framework for evaluating earthquake potential?. Geology 23, 629–632.
Parsons, T., Kaven, J.O., Velasco, A.A., Gonzalez-Huizar, H., 2006. Unraveling the apparent magnitude threshold of remote earthquake triggering using full wavefield surface wave simulation. Geochem. Geophys. Geosyst. 13 (6), Q06016, http://dx.doi.org/10.1029/2012GC004164.
Parsons, T., Velasco, A.A., 2011. Absence of remotely triggered large earthquakes beyond the mainshock region. Nat. Geosci. 4, 312–316.
Peng, Z., Gomberg, J., 2010. An integrated perspective of the continuum between earthquakes and slow-slip phenomena. Nat. Geosci. 3, 599–607.
Peng, Z., Vidale, J.E., Ishii, M., Helmstetter, A., 2007. Seismicity rate immediately before and after main shock rupture from high-frequency waveforms in Japan. J. Geophys. Res. 112, B03306, http://dx.doi.org/10.1029/2006JB004386.
Perfettini, H., Schmittbuhl, J., Cochard, A., 2003. Shear and normal load perturbations on a two-dimensional continuous fault: 2. Dynamic triggering. J. Geophys. Res. 108 (B9), 2409, http://dx.doi.org/10.1029/2002JB001805.
Pollitz, F.F., Stein, R.S., Sevilgen, V., Bürgmann, R., 2012. The 11 April 2012 east Indian Ocean earthquake triggered large aftershocks worldwide. Nature 490, 250–253.
Ratchkovski, N.A., Hansen, R.A., 2002. New constrains on tectonics of interior Alaska: earthquake locations, source mechanisms, and stress regime. Bull. Seismol. Soc. Am. 92, 998–1014.
Rondenay, S., Montési, L.G.J., Abers, G.A., 2010. New geophysical insight into the origin of the Denali volcanic gap. Geophys. J. Int. 182, 613–630.
Rubin, A.M., Ampuero, J.-P., 2005. Earthquake nucleation on (aging) rate and state faults. J. Geophys. Res. 110, B11312, http://dx.doi.org/10.1029/2005JB003686.
Rubinstein, J.L., Vidale, J.E., Gomberg, J., Bodin, P., Creager, K.C., Malone, S.D., 2007. Non-volcanic tremor driven by large transient shear stresses. Nature 448, 579–582.
Sagy, A., Brodsky, E.E., 2009. Geometric and rheological asperities in an exposed fault zone. J. Geophys. Res. 114, B02301, http://dx.doi.org/10.1029/2008JB005701.
Savage, H.M., Marone, C., 2008. Potential for earthquake triggering from transient deformations. J. Geophys. Res. 113, B05302, http://dx.doi.org/10.1029/2007JB005277.
Scholz, C.H., 2002. The Mechanics of Earthquakes and Faulting, 2nd ed. Cambridge University Press, Cambridge, UK.
Shearer, P.M., 2009. Introduction to Seismology, 2nd ed. Cambridge University Press, Cambridge, UK.
Shearer, P.M., Prieto, G.A., Hauksson, E., 2006. Comprehensive analysis of earthquake source spectra in southern California. J. Geophys. Res. 111, B06303, http://dx.doi.org/10.1029/2005JB003979.
Shelly, D.R., Peng, Z., Hill, D.P., Aiken, C., 2011. Triggered creep as a possible mechanism for delayed dynamic triggering of tremor and earthquakes. Nat. Geosci. 4, 384–388.
Tape, C., 2012. Assessment of Station Metadata in Alaska Based on Analysis of Love Waves from the 2012-04-11 M_w 8.6 Offshore Sumatra Earthquake, Version 3 (November 19, 2012). Alaska Earthquake Information Center Technical Report, available on-line, 36 pp.
Tape, W., Tape, C., 2012. Angle between principal axes triples. Geophys. J. Int. 191, 813–831.
Tromp, J., Komatitsch, D., Hjörleifsdóttir, V., Liu, Q., Zhu, H., Peter, D., Bozdag, E., McRitchie, D., Friberg, P., Trabant, C., Hutko, A., 2010. Near real-time simulations of global CMT earthquakes. Geophys. J. Int. 183, 381–389.
Van Kooten, G.K., Richter, M., Zippi, P.A., 2012. Alaska's Interior rift basins: a new frontier for discovery. Oil Gas J. 110 (1a) 10 pp.
Veenstra, E., Christensen, D.H., Abers, G.A., Ferris, A., 2006. Crustal thickness variation in south-central Alaska. Geology 34, 781–784.
Velasco, A.A., Hernandez, S., Parsons, T., Pankow, K., 2008. Global ubiquity of dynamic earthquake triggering. Nat. Geosci. 1, 375–379.
West, M., Sánchez, J.J., McNutt, S.R., 2005. Periodically triggered seismicity at Mount Wrangell, Alaska, after the Sumatra earthquake. Science 308, 1144–1146.
Wu, C., Peng, Z., Weng, W., Chen, Q.F., 2011. Dynamic triggering of shallow earthquakes near Beijing, China. Geophys. J. Int. 185, 1321–1334.
Zhu, L., Helmberger, D., 1996. Advancement in source estimation techniques using broadband regional seismograms. Bull. Seismol. Soc. Am. 86, 1634–1641.
Zhu, L., Rivera, L.A., 2002. A note on the dynamic and static displacements from a point source in multilayered media. Geophys. J. Int. 148, 619–627.
Zoback, M.D., Zoback, M.L., Mount, V.S., Suppe, J., Eaton, J.P., Healy, J.H., Oppenheimer, D., Reasenberg, P., Jones, L., Raleigh, C.B., Wong, I.G., Scotti, O., Wentworth, C., 1987. New evidence on the state of stress of the San Andreas fault system. Science 238, 1105–1111.